Journal of Materials Chemistry C

RSC Publishing

PAPER

View Article Online
View Journal | View Issue

# Nanogranular $Al_2O_3$ proton conducting films for low-voltage oxide-based homojunction thin-film transistors

Cite this: J. Mater. Chem. C, 2013, 1, 2781

Hongliang Zhang, Liqiang Guo and Qing Wan*

Nanogranular $Al_2O_3$ films were deposited by the plasma-enhanced chemical vapor deposition (PECVD) method using gas sources of trimethylaluminum and oxygen at 100 °C. Structural characterizations indicate that the as-deposited nanogranular $Al_2O_3$ film has an amorphous structure with excess oxygen due to ambient humidity and residual hydroxyl. As-deposited $Al_2O_3$ films show a mean pore size of 7.4 nm, and a high proton conductivity of $1.2 \times 10^{-4}$ S cm$^{-1}$ at room temperature with a 30% relative humidity. Low-voltage (1.5 V) indium-tin-oxide (ITO) thin-film transistors gated by such nanogranular $Al_2O_3$-based proton conductors exhibit a large current on/off ratio of $2.1 \times 10^7$ and a high field-effect mobility of 29 cm$^2$ V$^{-1}$ s$^{-1}$. Our results demonstrate that nanogranular $Al_2O_3$-based films are promising gate dielectric candidates for portable biosensors.

Received 5th December 2012
Accepted 20th February 2013

DOI: 10.1039/c3tc30137k

www.rsc.org/MaterialsC



## Introduction

Solid proton conducting materials have attracted much attention because of their potential practical applications in clean energy fields such as fuel cells,[1] batteries,[2] and chemical sensors.[3] Nafion, a very good organic proton conductor, has been widely investigated due to its potential for future fuel cell applications.[4–6] However, solution-processed organic proton conductors usually show a limited chemical stability and durability.[7,8] In contrast, inorganic oxide-based proton conductors are usually a chemically stable rigid solid. The surfaces of porous glasses and xerogels are terminated with hydroxyl bonds and absorb water from ambient air. The proton conductivity of these glasses is promoted by the dissociation of protons from hydroxyl groups and water molecules.[9–12] For the porous ceramics or glasses, the pore structure and surface chemicals are two important factors that influence the proton conductivity. A nanochannel filled with an acidic solution is thus a micro super proton conductor, and an array of such nanochannels forms an excellent proton conducting film.[13] Developing proton-driven smart nanopore/nanochannel materials is a scientific challenge with promising applications in biosensors, nanofluidic devices, molecular filtration, and energy conversion/storage.[14] An interesting feature of proton conductors is the ability to form so-called electric-double-layer (EDL) capacitors.[15] In thin-film transistors (TFTs) gated by proton conducting electrolytes, low-voltage operation is due to the large EDL capacitance at the electrolyte–gate electrode and the electrolyte–semiconducting channel interfaces.[16] Recently, an amorphous proton conducting mesoporous $Al_2O_3$ has been reported to show a high proton conductivity of $4.0 \times 10^{-3}$ S cm$^{-1}$ at 303 K with a 90% relative humidity (RH).[17] Furthermore, H. Shen *et al.* demonstrated that the proton conductivity of mesoporous $Al_2O_3$ can be improved by means of chloride-doping.[7] In the $SiO_2$ system, ions such as $P^{5+}$ and $H^+$ can be used to improve the proton conductivity of the sol–gel-derived porous glasses.[9–12] In general, mesoporous oxide films such as $Al_2O_3$ and $SiO_2$ were prepared by sol–gel and similar techniques.[7,10,17,18] However, such techniques involve a heating activation stage to get the final film, produce a substantial amount of waste materials, and generally lack uniformity in terms of film thickness and composition.[19–21]

In our previous work, as an alternative to the solution process, a conventional plasma-enhanced chemical vapor deposition (PECVD) process was used to facilitate the one-step deposition of nanoporous $SiO_2$-based proton conducting thin films at low temperature.[22] Here, we develop this simple PECVD process for nanogranular $Al_2O_3$ proton conducting thin film deposition. A high proton conductivity of $1.2 \times 10^{-4}$ S cm$^{-1}$ was obtained at room temperature with a low RH of 30%. Low voltage (1.5 V) indium-tin-oxide (ITO) TFTs gated by such nanogranular $Al_2O_3$-based proton conductors are self-assembled on glass substrates. Such low voltage TFTs are promising candidates for biosensors.

## Experimental

First, 460 nm thick nanogranular $Al_2O_3$ films were deposited on conducting ITO glass and Si (100) substrates by the PECVD method at 100 °C using a mixture of Ar, $O_2$ and

Ningbo Institute of Material Technology and Engineering, Chinese Academy of Sciences, Ningbo, 315201, People's Republic of China. E-mail: wanqing@nimte.ac.cn; Fax: +86 574 8669 0355; Tel: +86 574 8669 0355

trimethylaluminum (TMA) as the process gas under a working pressure of 50 Pa. Ar gas was used as a carrier gas for TMA. The Ar and $O_2$ were supplied into the chamber at flow rates of 4 sccm and 4 sccm, respectively. The power was fixed at 100 W using a 13.56 MHz RF source. Then, 200 nm thick ITO film for source–drain electrodes was deposited on the $Al_2O_3$ dielectric film at RT by RF magnetron sputtering of an ITO (10 wt% $SnO_2$ doped $In_2O_3$, 99.995%) target with a nickel shadow mask. ITO films were deposited in a 0.5 Pa pure Ar (99.995%) atmosphere with a RF power of 100 W. Here we should point out that a thin ITO channel can be self-assembled between the ITO source–drain electrodes due to the diffraction effect when the distance between the nickel shadow mask and the substrate is kept at ~50 μm. The channel width and length of the shadow mask is 1000 μm and 80 μm, respectively. The microstructures and the morphologies of the nanogranular $Al_2O_3$ film were analyzed by X-ray diffraction (XRD, Bruker AXS), field emission scanning electron microscopy (FESEM, Hitachi S-4800) and high resolution transmission electron microscopy (HRTEM, JEOL2100). The composition of the surface of the nanogranular $Al_2O_3$ thin film was characterized by X-ray photoelectron spectroscopy (XPS) (AXIS UTLTRA DLD) using Al Kα (1486.6 eV) radiation as an X-ray source with a voltage of 15 kV and a power of 120 W at a pressure of $\sim 5 \times 10^{-9}$ torr. The XPS spectra were recorded at the takeoff angle of ~90° relative to the surface. The samples were analyzed without sputter cleaning. The binding energies of the nanogranular $Al_2O_3$ thin film were corrected for surface charging using adventitious carbon $C_{1s}$ at 285 eV as a reference. The total energy resolution of this system was 0.48 eV. The total (chemisorbed + physisorbed) water content of the nanogranular $Al_2O_3$ was measured by thermogravimetric analysis (TGA) using a Perkin-Elmer, Model Pyris Diamond. Samples were equilibrated at 60% RH (relative humidity) before placing them in the balance crucible in order to reach full surface hydroxylation/hydration. TG curves were recorded under $N_2$ atmosphere of 50 sccm up to 500 °C at a heating rate of 10 °C $min^{-1}$. The nitrogen adsorption–desorption isotherm (ASAP 2020M, Micromeritics) was carried out at ~77 K to estimate the specific surface area and porous distribution by BET (Brunauer–Emmett–Teller) and BJH (Barret–Joyner–Halenda) methods. The content of Al–OH in the $Al_2O_3$ surface was calculated by analysis of the results of TGA and the BET surface area. An impedance analyzer (Solartron 1260) was employed for the $Al_2O_3$ thin film characterization. The electrical measurements of devices were carried out using a semiconductor parameter analyzer (Keithley 4200 SCS) at room temperature in the dark with a relative humidity (RH) of 30%.

## Results and discussion

Fig. 1(a) shows an XRD pattern of the $Al_2O_3$ film. XRD analysis indicates that the $Al_2O_3$ film has an amorphous characteristic. Fig. 1(b) shows the cross-section SEM image of the 460 nm thick $Al_2O_3$ film deposited on the Si substrate. Compact nanoparticles

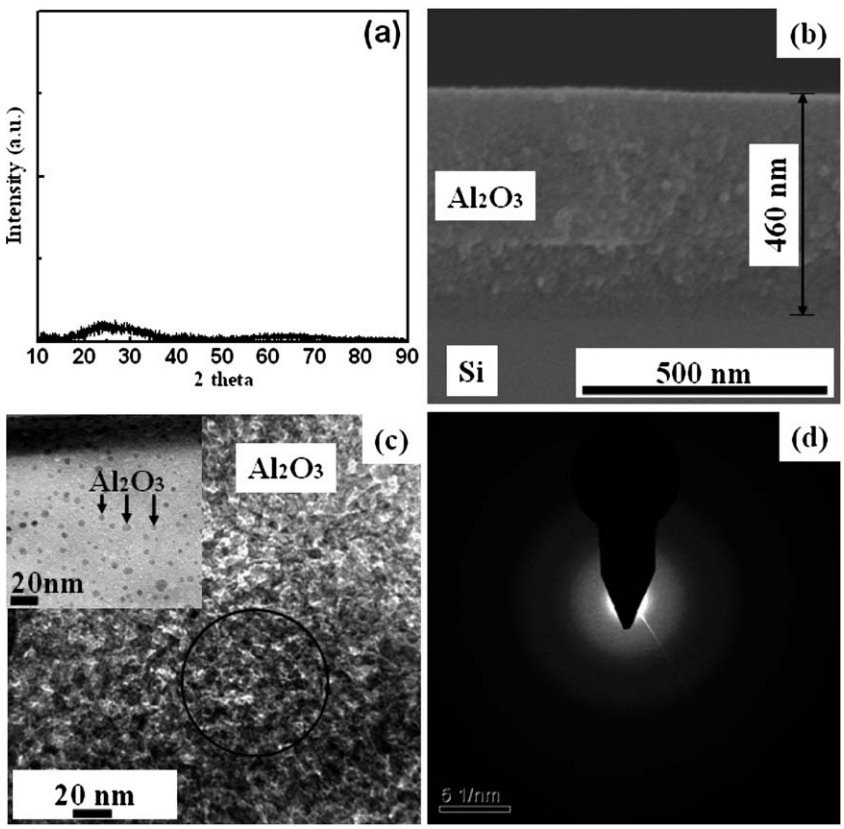


**Fig. 1** (a) XRD pattern of the nanogranular $Al_2O_3$ film deposited by the PECVD method. (b) SEM image of the cross-section view of the $Al_2O_3$ film deposited on a crystalline Si substrate. (c) HRTEM images, and (d) the SAED pattern of the nanogranular $Al_2O_3$ thin film deposited on the Cu grid.

 

with a mean size of less than 10 nm and a globular morphology were seen in the film. Fig. 1(c) and (d) show the HRTEM images and the selected area electron diffraction (SAED) pattern of the very thin nanogranular $Al_2O_3$ thin film deposited on the Cu grid for TEM. It shows a worm-like structure with irregularly aligned nanopores. The inset of Fig. 1(c) shows some divided nanoparticles with a diameter of 2–8 nm. Some nanoparticles (the encircled area in Fig. 1(c)) produce diffused halo rings in the SAED pattern, indicating amorphous structural characteristic. Based on the XRD, SEM, HRTEM and SAED results, we can get the conclusion that the as-deposited $Al_2O_3$ thin film is composed of nanoparticles with an amorphous structure, which is favorable for proton conduction.

Fig. 2(a) and (b) show the deconvoluted $O_{1s}$ at 531 eV and $Al_{2p}$ at 73.6 eV XPS spectra of the surface of the nanogranular $Al_2O_3$ thin film. The deconvoluted $O_{1s}$ spectra can see two major components of 530.55 eV and 531.85 eV, respectively, which are consistent with Al–O–Al and Al–O–H environments.[23] Also, a weak peak component (less than 1% of the total $O_{1s}$ area) at 533.55 eV is assigned to adsorbed water molecules. The two peak components around 73.25 eV and 74.7 eV are observed, which are ascribed to O–Al–O and O–Al–O–H binding energies of the surface of the nanogranular $Al_2O_3$ thin film, respectively.[23] After Shirley background subtraction, the relative atomic concentration ratio of O and Al is derived from the individual peak areas since the associated relative sensitivity factors ($RSF_{O1s}$: 0.78 and $RSF_{Al2p}$: 0.193) are known. According to the calculation $((I_{O1s}/RSF_{O1s}) : (I_{Al2p}/RSF_{Al2p}))$, the atomic concentration ratio O : Al is approximately 2.6 : 1. The calculated value is more than the theoretical stoichiometric proportion 1.5 : 1, due to the surface chemisorption oxygen species of the nanogranular $Al_2O_3$ thin film. The absorbed oxygen species originate from hydroxyl groups, which form on the nanogranular $Al_2O_3$ surface due to atmospheric humidity and residual hydroxyl.

Fig. 3(a) shows the TG curve of the nanogranular $Al_2O_3$ sample in a $N_2$ atmosphere. The total weight loss of physically and chemically absorbed water at temperatures between 50 and 300 °C in a $N_2$ atmosphere was 8%. Fig. 3(b) shows the typical nitrogen sorption isotherm and pore size distribution of the nanogranular $Al_2O_3$. Pore size distribution of the $Al_2O_3$ was calculated by the BJH method from the nitrogen sorption isotherm. It can be seen that the $Al_2O_3$ deposited by the low temperature PECVD method is nanoporous, with a BET surface area of $35.4 \pm 0.17$ $m^2$ $g^{-1}$ and an average pore diameter of $7.4 \pm 0.001$ nm. The nanopore–nanochannel structures of the $Al_2O_3$ result from the array and close-packing of $Al_2O_3$ nanoparticles. From TG results the number of total water molecules per unit of specific surface area was calculated. These calculations show that at 60% RH and from 50 to 300 °C the total number of water molecules (chemisorbed + physisorbed) per square nanometer is 76 molecules per $nm^2$, which is higher than the value (32 molecules per $nm^2$) of the proton conducting mesoporous hematite ceramic.[24]

The proton conductivity of the nanogranular $Al_2O_3$ film was determined from Cole–Cole plots by an AC method using a Solartron 1260 impedance analyzer at 30% RH. The Cole–Cole plot consisted of a single semicircle and the proton conductivity was obtained from the intersecting point of the semicircle with

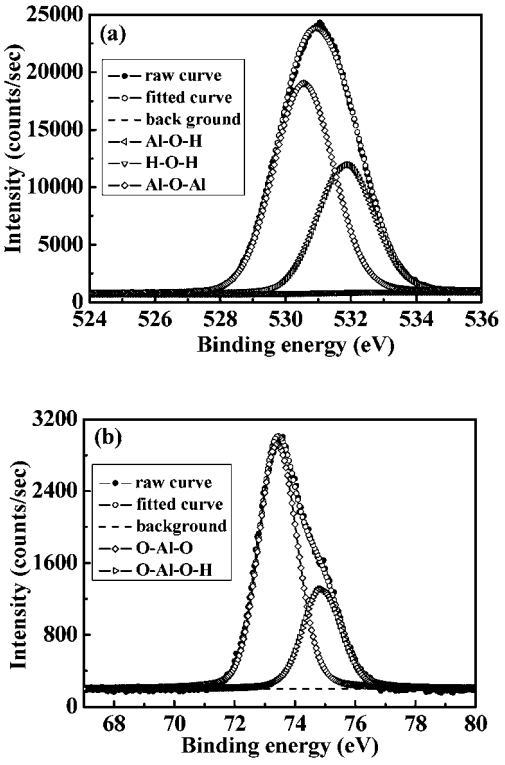


**Fig. 2** Deconvoluted (a) $O_{1s}$ and (b) $Al_{2p}$ spectra of the surface of the nanogranular $Al_2O_3$ film, respectively.

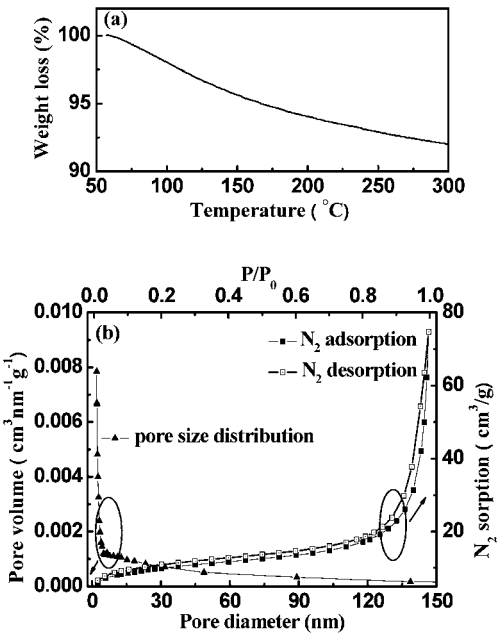


**Fig. 3** (a) TG curve of the nanogranular $Al_2O_3$ under $N_2$ atmosphere. (b) Nitrogen adsorption–desorption isotherm and pore size distribution of the nanogranular $Al_2O_3$.

the real axis, as shown in Fig. 4(a). The proton conductivity, $\sigma$, was calculated from $R$ and pellet dimension, *i.e.*, $\sigma = L/(R - R_0)A$,[25] where $L$, $A$ and $R_0$ are the thickness of the $Al_2O_3$ film, the electrode surface area and the rig short circuit resistance, respectively. The proton conductivity of the $Al_2O_3$ electrolyte film is calculated to be $1.2 \pm 0.06 \times 10^{-4}$ S cm$^{-1}$ ($R_0 = 30$ Ohm). The high proton conductivity indicates that absorbed water facilitates proton conduction by means of a nanochannel-induced proton conduction enhancement effect.[13] Inset of Fig. 4(a) depicts the current leakage curve of the $Al_2O_3$ film in the bias voltage between +2.0 V and −1.5 V. A relatively low gate leakage current of ~1.0 nA was obtained, which is much lower than that (~100 nA) of organic TFTs gated by ion gel gate dielectrics.[26] The channel on-current (~300 μA) is five orders of magnitude larger than the leakage current, which guarantees that our device performance will not be affected by the leakage. As a result, our device is acceptable for sensor applications.

Fig. 4(b) shows the specific gate capacitance of the $Al_2O_3$ film in the frequency range of 1.0 Hz–1.0 MHz. The specific gate capacitance ($C_i$) at 1 Hz was determined to be 1.95 μF cm$^{-2}$, which is ~108 times larger than the theoretically calculated value (taking the dielectric constant of $Al_2O_3$ as 9 and the thickness of 460 nm, the specific capacitance of $Al_2O_3$ dielectric should be 0.018 μF cm$^{-2}$, according to the plate specific capacitance equation: $C_i = \varepsilon_0\varepsilon_r/d$). Similar to the results reported by Oscar Larsson *et al.*,[27] the capacitive behavior at low frequencies is associated with the formation of an electric-double-layer (EDL) at $Al_2O_3$–ITO electrode interfaces. Based on the value of the phase angle, the relaxation phenomena can be classified either with a capacitive ($\theta(f) < -45°$) or resistive ($\theta(f) > -45°$) behavior. The capacitance–frequency characteristic of the nanogranular $Al_2O_3$ proton conductors can be divided into the following three different frequency regions: (1) the capacitive behavior at high frequencies is attributed to dipolar relaxation of the nanogranular $Al_2O_3$; (2) the resistive behavior at intermediate frequencies originates from dissociated protons migrating away from the nanogranular $Al_2O_3$ film in the oscillating electric field. This is called ionic relaxation and (3) the capacitive behavior at low frequencies is associated with the formation of EDL at the nanogranular $Al_2O_3$ film–ITO electrode interfaces.

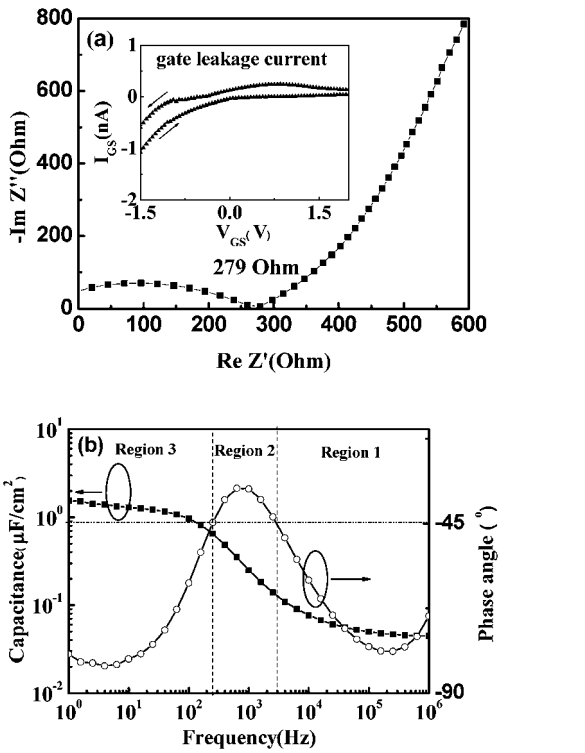


**Fig. 4** (a) Typical Cole–Cole plot and (b) the specific capacitance *versus* frequency characteristics measured at 30% RH at room temperature with an ITO–$Al_2O_3$–ITO sandwich test structure for the $Al_2O_3$ proton conductor. Inset: gate leakage current of the $Al_2O_3$ film.

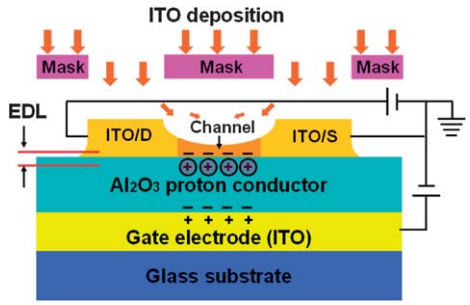


**Fig. 5** A schematic cross-section of a self-assembled ITO TFT gated by the nanogranular $Al_2O_3$ proton conductor under a positive gate bias stress.

Fig. 5 shows the schematic diagram of a self-assembled ITO-based TFT gated by the nanogranular $Al_2O_3$ proton conductor on the transparent conducting glass substrate. Only one shadow mask is needed for such device fabrication because the patterned ITO channel can be self-aligned between ITO source–drain electrodes simultaneously during the one-step RF sputtering process. Here, we should point out that a proper mask-to-substrate distance must be chosen to precisely control the thickness and uniformity of the active channel. Here, the distance between the mask and the substrate during deposition is about 50 μm. If the distance was too small, the self-assembled channel would gradually disappear. If the distance was too large, the self-assembled channel would be too thick to be used as the channel.

Fig. 6(a) shows the typical output characteristics ($I_{DS}$–$V_{DS}$) of the ITO-based homojunction TFTs gated by the nanogranular $Al_2O_3$ film. The $V_{GS}$ was varied from −0.6 to 0.8 V in 0.2 V steps. The curves exhibit good current saturation behaviors at high $V_{DS}$ and linear characteristics of $I_{DS}$ at low $V_{DS}$. Fig. 6(b) shows the corresponding transfer characteristics of the device at a fixed $V_{DS} = 1.6$ V. Such a transistor exhibits a high-performance with a large drain current on/off ratio of $2.1 \times 10^7$ and a small subthreshold swing of 110 mV per decade, respectively. A threshold voltage ($V_{th}$) of −0.31 V was calculated from the $x$-axis intercept of the square root of the $I_{DS}$-*versus*-$V_{GS}$ plot. The field-effect mobility ($\mu_{FET}$) in the saturation region ($V_{DS} > V_{GS} - V_{th}$) can be derived from the following equation: $I_{DS} = (WC_i\mu/2L)(V_{GS} - V_{th})^2$, where $L = 80$ μm is the channel length, $W = 1000$ μm is the channel width, and $C_i$ is the specific gate capacitance.

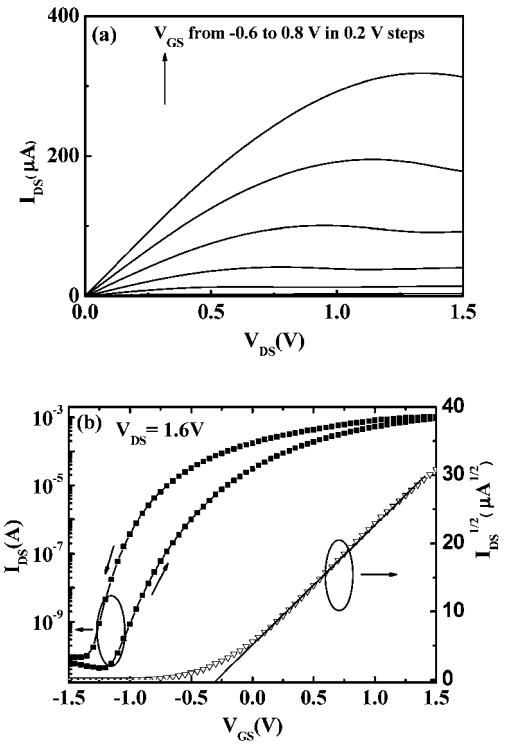


**Fig. 6** Electrical characteristics of the ITO TFTs gated by the nanogranular $Al_2O_3$ proton conductor. (a) Output characteristics. $V_{DS}$ was swept from 0 to 1.5 V at each $V_{GS}$ that varied from −0.6 to 0.8 V at 0.2 V steps. (b) Transfer characteristics at a fixed $V_{DS}$ = 1.6 V.

The field-effect mobility was calculated to be as high as 29 $cm^2\ V^{-1}\ s^{-1}$.

Fig. 7 shows the transient response of a device to a square-shaped $V_{GS}$ with a pulsed amplitude of $V_+ = 1.5$ V and $V_- = -1.5$ V. The device exhibits a good reproducibility of current response to the repeatedly pulsed $V_{GS}$. This strongly suggests that there was no chemical doping at the $Al_2O_3$–ITO interface when the gate potential is biased, because if chemical doping had occurred, $I_{DS}$ would not have returned to its original value after gate scanning.

It was reported that oxide-based TFTs gated by a normal 150 nm thick $Al_2O_3$ film without nanostructures showed an operation voltage of 25 V.[28] Recently, IGZO TFTs gated by a 30 nm thick $Al_2O_3$ film still showed an operation voltage of 5.0 V.[29] The low-voltage operation mechanisms of the ITO-based TFTs gated by $Al_2O_3$ proton conducting films can be explained as follows. When a positive voltage is applied at the bottom gate electrode, mobile protons ($H^+$) in the $Al_2O_3$-based proton conducting film will move to the area near the interface of the top self-assembled ITO channel and form an interfacial EDL as shown in Fig. 5. The EDL at the channel interface, regarded as a nanogap capacitor with a huge capacitance, can accumulate electrons in the channel to a very high density level which is impossible for conventional dense gate dielectrics. When the gate voltage is shifted to the negative direction, the ITO channel can be gradually depleted by the large EDL capacitance. The nanoporous structure and proton conducting properties of the $Al_2O_3$ film is the determinant reason for low voltage (1.5 V) operation. So nanogranular $Al_2O_3$-based films are promising gate dielectric candidates for low-voltage portable oxide-based electronics.

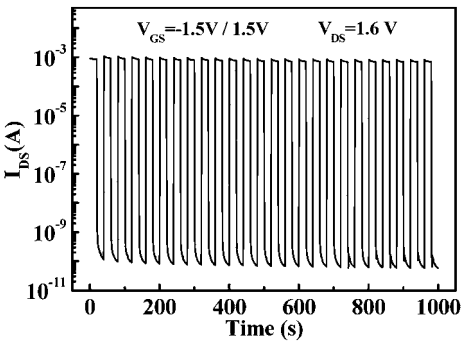


**Fig. 7** Time response of the ITO TFTs gated by the nanogranular $Al_2O_3$ proton conductor to a pulsed square-shaped gate voltage with a pulsed amplitude of $V_+ = 1.5$ V and $V_- = -1.5$ V.

## Conclusions

In summary, nanogranular $Al_2O_3$ films were deposited by the PECVD method at 100 °C using trimethylaluminum and $O_2$ as the reactive gases. Structural characterizations indicate that the as-deposited nanogranular $Al_2O_3$ film has an amorphous structure with excess oxygen due to ambient humidity and residual hydroxyl. The $Al_2O_3$ film shows a mean pore size of 7.4 nm and a total absorbed water number of 76 molecules per square nanometer. A high proton conductivity of $1.2 \times 10^{-4}$ S $cm^{-1}$ was measured at room temperature with a RH of 30%. Low-voltage (1.5 V) ITO-based TFTs gated by such a nanoporous $Al_2O_3$ proton conductor have a large current on/off ratio of $2.1 \times 10^7$, a low subthreshold swing of 110 mV per decade and a high field-effect mobility 29 $cm^2\ V^{-1}\ s^{-1}$. Such low-voltage oxide-based EDL TFTs are suitable for applications in biosensors.

## Acknowledgements

This project is supported by the National Program on Key Basic Research Project (2012CB933004), the National Natural Science Foundation of China (11174300), and the Fok Ying Tung Education Foundation (Grant no. 121063).

## References

1 B. P. Tripathi and V. K. Shahi, *Prog. Polym. Sci.*, 2011, **36**(7), 945.
2 N. Lakshmi and S. Chandra, *J. Power Sources*, 2002, **108**(1–2), 256.
3 N. Fukatsu and N. Kurita, *Ionics*, 2007, **13**(3), 183.
4 N. Miyake, J. S. Wainright and R. F. Savinell, *J. Electrochem. Soc.*, 2001, **148**(8), A905.
5 J. Shen, J. Xi, W. Zhu, L. Chen and X. Qiu, *J. Power Sources*, 2006, **159**(2), 894.
6 G. G. Kumar, P. Kim, K. s. Nahm and R. N. Elizabeth, *J. Membr. Sci.*, 2007, **303**(1–2), 126.

7 H. Shen, H. Maekawa, L. Wang, B. Guo and K. Shu, *Electrochem. Solid-State Lett.*, 2009, **12**(2), B18.
8 Z. Li and T. Tang, *Solid State Ionics*, 2012, **211**, 34.
9 Y. Abe, H. Hosono, Y. Ohta and L. Hench, *Phys. Rev. B: Condens. Matter Mater. Phys.*, 1988, **38**(14), 10166.
10 M. Nogami, R. Nagao, G. Wong, T. Kasuga and T. Hayakawa, *J. Phys. Chem. B*, 1999, **103**(44), 9468.
11 M. Nogami, Y. Goto, Y. Tsurita and T. Kasuga, *J. Am. Ceram. Soc.*, 2001, **84**(11), 2553.
12 A. Matsuda, T. Kanzaki, K. Tadanaga, T. Kogure, M. Tatsumisago and T. Minami, *J. Electrochem. Soc.*, 2002, **149**(8), E292.
13 S. R. Liu, Q. S. Pu, L. Gao, C. Korzeniewski and C. Matzke, *Nano Lett.*, 2005, **5**(7), 1389.
14 X. Hou, W. Guo and L. Jiang, *Chem. Soc. Rev.*, 2011, **40**, 2385.
15 N. Kaihovirta, H. Aarnio, C.-J. Wikman, C.-E. Wilén and R. Österbacka, *Adv. Funct. Mater.*, 2010, **20**, 2605.
16 L. Herlogsson, X. Crispin, N. D. Robinson, M. Sandberg, O. J. Hagel, G. Gustafsson and M. Berggren, *Adv. Mater.*, 2007, **19**, 97.
17 H. Shen, H. Maekawa, J. Kawamura and T. Yamamura, *Solid State Ionics*, 2006, **177**(26–32), 2403.
18 T. Uma, K. Hattori and M. Nogami, *Ionics*, 2005, **11**(3–4), 202.
19 A. Borrás, A. Barranco and A. R. González-Elipe, *J. Mater. Sci.*, 2006, **41**(16), 5220.
20 P. Y. Liu, J. F. Chen and W. D. Sun, *Vacuum*, 2004, **76**(1), 7.
21 M. Macias-Montero, A. Borras, Z. Saghi, J. P. Espinos, A. Barranco, J. Cotrino and A. R. Gonzalez-Elipe, *Nanotechnology*, 2012, **23**(25), 255303.
22 J. Sun, J. Jiang, A. Lu, B. Zhou and Q. Wan, *IEEE Trans. Electron Devices*, 2011, **58**(3), 764.
23 M. R. Alexander, G. E. Thompson and G. Beamson, *Surf. Interface Anal.*, 2000, **29**(7), 468.
24 M. T. Colomer, *J. Power Sources*, 2011, **196**(20), 8280.
25 Y. Jin, S. Qiao, J. C. D. da Costa, B. J. Wood, B. P. Ladewig and G. Q. Lu, *Adv. Funct. Mater.*, 2007, **17**(16), 3304.
26 J. H. Cho, J. Lee, Y. He, B. S. Kim, T. P. Lodge and C. D. Frisbie, *Adv. Mater.*, 2008, **20**(4), 686.
27 O. Larsson, E. Said, M. Berggren and X. Crispin, *Adv. Funct. Mater.*, 2009, **19**(20), 3334.
28 J. Sun, D. A. Mourey, D. Zhao and T. N. Jackson, *J. Electron. Mater.*, 2007, **37**(5), 755.
29 C.-H. Wu, K.-M. Chang, S.-H. Huang, I. C. Deng, C.-J. Wu, W.-H. Chiang and C.-C. Chang, *IEEE Electron Device Lett.*, 2012, **33**(4), 552.

 